nature nanotechnology

ARTICLES

PUBLISHED ONLINE: 2 MARCH 2014 | DOI: 10.1038/NNANO.2014.15

An antidamping spin–orbit torque originating from the Berry curvature

H. Kurebayashi[1,2†], Jairo Sinova[3,4,5], D. Fang[1], A. C. Irvine[1], T. D. Skinner[1], J. Wunderlich[5,6], V. Novák[5], R. P. Campion[7], B. L. Gallagher[7], E. K. Vehstedt[4,5], L. P. Zârbo[5], K. Výborný[5], A. J. Ferguson[1]* and T. Jungwirth[5,7]

Magnetization switching at the interface between ferromagnetic and paramagnetic metals, controlled by current-induced torques, could be exploited in magnetic memory technologies. Compelling questions arise regarding the role played in the switching by the spin Hall effect in the paramagnet and by the spin–orbit torque originating from the broken inversion symmetry at the interface. Of particular importance are the antidamping components of these current-induced torques acting against the equilibrium-restoring Gilbert damping of the magnetization dynamics. Here, we report the observation of an antidamping spin–orbit torque that stems from the Berry curvature, in analogy to the origin of the intrinsic spin Hall effect. We chose the ferromagnetic semiconductor (Ga,Mn)As as a material system because its crystal inversion asymmetry allows us to measure bare ferromagnetic films, rather than ferromagnetic–paramagnetic heterostructures, eliminating by design any spin Hall effect contribution. We provide an intuitive picture of the Berry curvature origin of this antidamping spin–orbit torque as well as its microscopic modelling. We expect the Berry curvature spin–orbit torque to be of comparable strength to the spin-Hall-effect-driven antidamping torque in ferromagnets interfaced with paramagnets with strong intrinsic spin Hall effect.

In one interpretation discussed in the literature so far, current-induced switching at ferromagnet/paramagnet interfaces[1,2] originates from an antidamping component of the spin–orbit torque (SOT)[1,3–24] at the broken space-inversion-symmetry interface, while in another[2,23,25], the spin Hall effect (SHE)[26–32] in the paramagnet combines with the antidamping spin-transfer torque (STT)[33–36] in the ferromagnet. Because, so far, the theories have considered a scattering-related SOT with an antidamping component that is expected to be relatively weak compared with the field-like SOT component[18,19], much attention has been focused on the SHE–STT interpretation, in which the large SHE originates from the Berry curvature in the band structure of a clean crystal[2,28,29,37]. The focus of the present work is on a large antidamping SOT that stems from a Berry curvature origin analogous to intrinsic SHE.

In conventional semiclassical transport theory, the linear response of the carrier system to the applied electric field is described by the non-equilibrium distribution function of carrier eigenstates, which are considered to be unperturbed by the electric field. The form of the non-equilibrium distribution function is obtained by accounting for the combined effects of the carrier acceleration in the field and of scattering. For the SOT, the non-equilibrium distribution function can be used to evaluate the current-induced carrier spin density, which then exerts the torque on the magnetization via carrier–magnetic moment exchange coupling. The field-like component of the SOT reported in previous theoretical and experimental studies in (Ga,Mn)As films[4,8,9,11,24] and predicted for interfaces with broken structural inversion symmetry[5,6] is described within this theory framework. Scattering-related mechanisms were also considered to generate an antidamping-like component of the SOT in the transition-metal multilayers[17–20]. In ref. 17, the antidamping-like SOT term arises from the electron scattering-induced spin relaxation. In ref. 20, the semiclassical diffusion formalism was used, whereas in refs 18,19 the antidamping-like SOT is obtained within a quantum kinetic formalism and ascribed to spin-dependent carrier lifetimes[18] or to a term arising from the weak-diffusion limit, which in the leading order is proportional to a constant carrier lifetime[19]. Furthermore, in ref. 18, a connection is made between these scattering-related antidamping SOT theories and the out-of-plane spin polarization resulting from the interplay between spin–orbit interaction and external electric and magnetic fields in a non-magnetic two-dimensional Rashba system in the presence of anisotropic impurity scattering[38].

Unlike transport theories based on evaluating the non-equilibrium distribution function, in time-dependent quantum-mechanical perturbation theory the linear response is described by the equilibrium distribution function and by the perturbation of carrier wavefunctions in the applied electric field. This latter framework formed the basis for the intrinsic Berry curvature mechanism originally introduced to explain the anomalous Hall effect in the ferromagnetic semiconductor (Ga,Mn)As (ref. 39) and, subsequently, also in a number of common transition-metal ferromagnets[40]. Via the anomalous Hall effect, Berry curvature physics entered the field of the SHE, where studies again initially focused on the spin–orbit coupled semiconductor structures due to their relatively simple band structure and, subsequently, included the spin–orbit coupled metal paramagnets. The concept of a scattering-independent origin attracted the attention of a wide physics community to this relativistic phenomenon,

[1]Microelectronics Group, Cavendish Laboratory, University of Cambridge, JJ Thomson Avenue, Cambridge CB3 0HE, UK, [2]PRESTO, Japan Science and Technology Agency, Kawaguchi 332-0012, Japan, [3]Institut für Physik, Johannes Gutenberg-Universität Mainz, 55128 Mainz, Germany, [4]Department of Physics, Texas A&M University, College Station, Texas 77843-4242, USA, [5]Institute of Physics ASCR, v.v.i., Cukrovarnická 10, 162 53 Praha 6, Czech Republic, [6]Hitachi Cambridge Laboratory, Cambridge CB3 0HE, UK, [7]School of Physics and Astronomy, University of Nottingham, Nottingham NG7 2RD, UK, †Present address: London Centre for Nanotechnology, UCL, 17–19 Gordon Street, WC1H 0AH, UK. *e-mail: ajf1006@cam.ac.uk

eventually turning the SHE into an important field of condensed matter physics and spintronics[32].

In recent experiments it has been argued that the intrinsic SHE[2,28,29,37], combined with the STT, explains the symmetry and approximate magnitude of the observed in-plane current-induced magnetization switching at ferromagnet/paramagnet metal interfaces. Here, we demonstrate that there is an intrinsic antidamping SOT that has the relativistic quantum-mechanical Berry curvature origin as the intrinsic SHE. In this initial study of the intrinsic antidamping SOT we focus on (Ga,Mn)As, taking advantage again of the strong spin–orbit coupling and simple band structure of this ferromagnetic semiconductor. In the case of the SOT, (Ga,Mn)As provides yet another essential advantage, compared to, for example, common metals, allowing us to readily isolate this new SOT from the SHE–STT mechanism. The zinc-blende crystal structure of (Ga,Mn)As lacks bulk space-inversion symmetry, which makes it possible to study the SOT phenomena in a bare ferromagnetic semiconductor film[8,10,11]. Because no conducting paramagnet is interfaced with our (Ga,Mn)As film, the SHE–STT mechanism is excluded by design.

Theory of the Berry curvature antidamping SOT

We start by deriving the intuitive picture of our Berry curvature antidamping SOT based on the Bloch equation description of the carrier spin dynamics. In (Ga,Mn)As, the combination of the broken inversion symmetry of the zinc-blende lattice and strain can produce spin–orbit coupling terms in the Hamiltonian that are linear in momentum and have the Rashba symmetry, $H_R = \frac{\alpha}{\hbar}(\sigma_x p_y - \sigma_y p_x)$, or the Dresselhaus symmetry, $H_D = \frac{\beta}{\hbar}(\sigma_x p_x - \sigma_y p_y)$ (Fig. 1a)[8–11]. Here, σ represents the Pauli spin matrices, α and β are the strengths of the Rashba and Dresselhaus spin–orbit coupling, respectively, $p_{x,y}$ are the momenta in the epilayer plane, and $\hbar$ is the reduced Planck constant. The interaction between carrier spins and magnetization is described by the exchange Hamiltonian term, $H_{ex} = J\sigma\cdot\mathbf{M}$. In (Ga,Mn)As, $\mathbf{M}$ corresponds to the ferromagnetically ordered local moments on the Mn d orbitals and J is the antiferromagnetic carrier–local moment kinetic-exchange constant[41]. The physical origin of our antidamping SOT is best illustrated assuming, for simplicity, a two-dimensional parabolic form of the spin-independent part of the total Hamiltonian, $H = \frac{p^2}{2m} + H_{R(D)} + H_{ex}$ and the limit of $H_{ex} \gg H_{R(D)}$, where m is the mass of the charge carriers. In equilibrium, the carrier spins are then approximately aligned with the exchange field, independent of their momentum. The origin of the SOT can be understood from solving the Bloch equations for carrier spins during the acceleration of the carriers in the applied electric field, that is, between the scattering events. Let us define the x-direction as the direction of the applied electric field $\mathbf{E}$. For $-\mathbf{M}\|\mathbf{E}$, the equilibrium effective magnetic field acting on the carrier spins, $\mathbf{s} = \frac{\sigma}{2}$, due to the exchange term is, $\mathbf{B}_{eff}^{eq} \approx (2JM, 0, 0)$, in units of energy. During the acceleration in the applied electric field, $dp_x/dt = eE_x$ (t is time and e is the carrier charge), and the effective magnetic field acquires a time-dependent y-component due to H_R for which $\frac{dB_{eff,y}}{dt} = \frac{2\alpha}{\hbar}\frac{dp_x}{dt}$, as illustrated in Fig. 1b. For small tilts of the spins from equilibrium, the Bloch equations $\frac{d\mathbf{s}}{dt} = \frac{1}{\hbar}(\mathbf{s} \times \mathbf{B}_{eff})$ yield, $s_x \approx s$, $s_y \approx s(B_{eff,y}/B_{eff}^{eq})$ and

$$s_z \approx -\frac{\hbar s}{(B_{eff}^{eq})^2}\frac{dB_{eff,y}}{dt} = -\frac{s}{2J^2M^2}\alpha e E_x \qquad (1)$$

The non-equilibrium spin orientation of the carriers acquires a time- and momentum-independent s_z component.

As illustrated in Fig. 1b,c, s_z depends on the direction of the magnetization $\mathbf{M}$ with respect to the applied electric field. It has a maximum for $\mathbf{M}$ (anti)parallel to $\mathbf{E}$ and vanishes for $\mathbf{M}$ perpendicular to $\mathbf{E}$. For a general angle, $\theta_{\mathbf{M}-\mathbf{E}}$, between $\mathbf{M}$ and $\mathbf{E}$ we obtain

$$s_{z,\mathbf{M}} \approx \frac{s}{2J^2M^2}\alpha e E_x \cos\theta_{\mathbf{M}-\mathbf{E}} \qquad (2)$$

The total non-equilibrium spin polarization, $S_z = 2g_{2D}JMs_{z,\mathbf{M}}$, is obtained by integrating $s_{z,\mathbf{M}}$ over all occupied states (g_{2D} is the density of states). The non-equilibrium spin polarization produces an out-of-plane field that exerts a torque on the in-plane magnetization. From equation (2) we obtain that this intrinsic SOT is antidamping-like:

$$\frac{d\mathbf{M}}{dt} = \frac{J}{\hbar}(\mathbf{M} \times S_z\hat{z}) \sim \mathbf{M} \times ([\mathbf{E} \times \hat{z}] \times \mathbf{M}) \qquad (3)$$

For the Rashba spin–orbit coupling, equation (3) applies to all directions of the applied electric field with respect to the crystal axes. For Dresselhaus spin–orbit coupling, the symmetry of the antidamping SOT depends on the direction of $\mathbf{E}$ with respect to the crystal axes. In Table 1 we summarize the angle dependence of the Rashba and Dresselhaus contributions to S_z for electric fields along different crystal directions. (Note that in the case of the magnetization aligned in the out-of-plane direction, the Berry curvature non-equilibrium spin-polarization component will have an in-plane direction, with the in-plane angle depending on the form of the spin–orbit Hamiltonian and on the current direction.)

To highlight the analogy in microscopic mechanisms but also the distinct phenomenologies of our antidamping SOT and the intrinsic Berry curvature SHE[28,29], we illustrate in Fig. 1d the solution of the Bloch equations in the absence of the exchange Hamiltonian term[29]. In this case, $\mathbf{B}_{eff}^{eq}$ depends on the angle $\theta_{\mathbf{p}}$ of the carrier momentum with respect to $\mathbf{E}$, which implies a momentum-dependent z-component of the non-equilibrium spin,

$$s_{z,\mathbf{p}} \approx \frac{s\hbar^2}{2\alpha p^2}\alpha e E_x \sin\theta_{\mathbf{p}} \qquad (4)$$

Clearly, the same spin rotation mechanism that generates the uniform bulk spin accumulation in the case of our antidamping SOT in a ferromagnet (Fig. 1b) is responsible for the scattering-independent spin current of the SHE in a paramagnet (Fig. 1d). Note that the SHE spin current yields zero spin accumulation in the bulk, and a net spin polarization can occur only at the edges of the paramagnet.

To complete the picture of the common origin between the microscopic physics of the Berry curvature SHE and our antidamping SOT, we point out that analogous expressions for the SHE spin current and the SOT spin polarization can be obtained from the quantum-transport Kubo formula. The expression for the out-of-plane non-equilibrium spin polarization that generates our antidamping SOT is given by

$$S_z = \frac{\hbar}{V}\sum_{\mathbf{k},a\neq b}(f_{\mathbf{k},a} - f_{\mathbf{k},b})\frac{\mathrm{Im}[\langle\mathbf{k},a|s_z|\mathbf{k},b\rangle\langle\mathbf{k},b|e\mathbf{E}\cdot\mathbf{v}|\mathbf{k},a\rangle]}{(E_{\mathbf{k},a} - E_{\mathbf{k},b})^2} \qquad (5)$$

where $\mathbf{k}$ is the wavevector, a and b are the band indices, $\mathbf{v}$ is the velocity operator, V is the volume and $f_{\mathbf{k},a}$ is the Fermi–Dirac distribution function corresponding to band energies $E_{\mathbf{k},a}$. This expression is analogous to equation (9) in ref. 29 for the Berry curvature intrinsic SHE.

Measurement of antidamping SOT in (Ga,Mn)As

Previous studies of the SOT in (Ga,Mn)As epilayers have focused on the scattering-related, field-like SOT generated by the in-plane component of the non-equilibrium spin polarization of carriers[8,9,11]. We

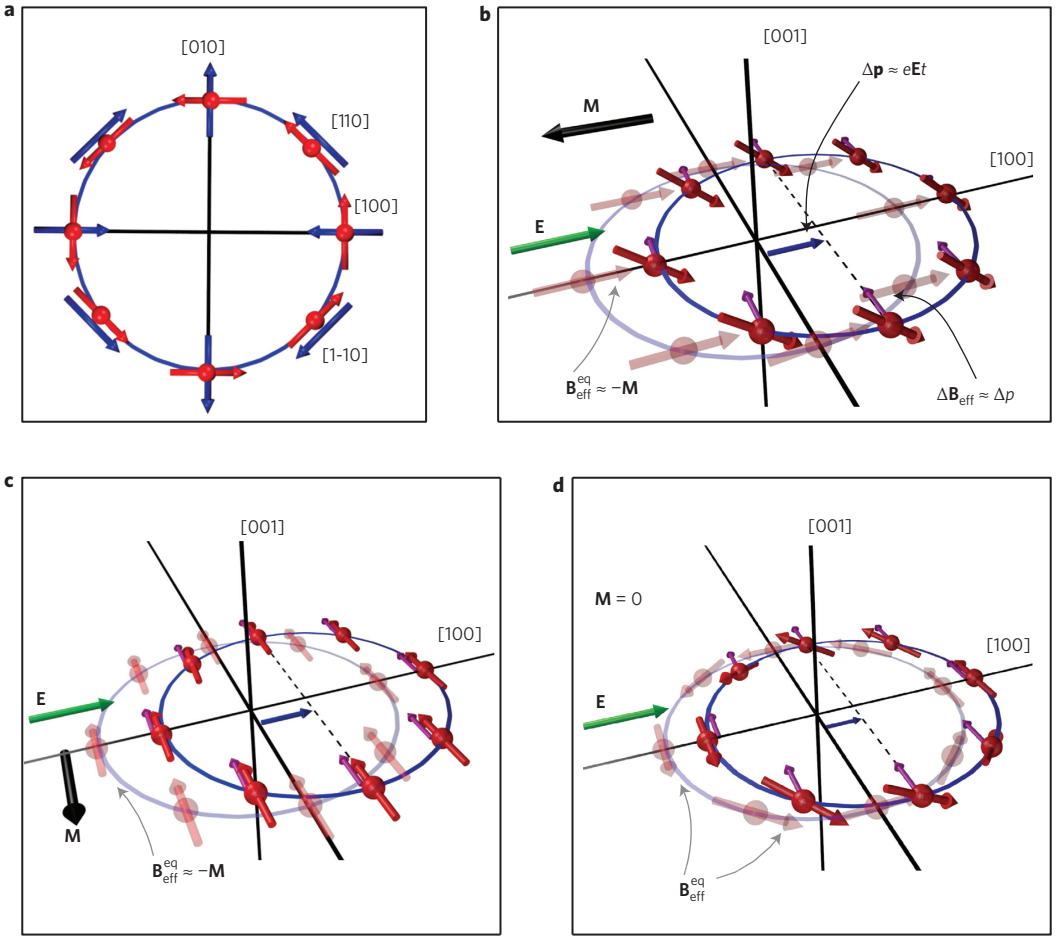

Figure 1 | Spin–orbit coupling and antidamping SOT. a, Rashba (red) and Dresselhaus (blue) fields for momenta along different crystallographic directions. **b**, Semitransparent regions represent the equilibrium configuration in which the carrier spins experience an equilibrium effective field $\mathbf{B}_{\mathrm{eff}}^{\mathrm{eq}}$, which anti-aligns them to the magnetization **M** (black arrow). During acceleration by the applied electric field **E** (green arrow), which shifts the centre of the Fermi surface by $\Delta\mathbf{p} \approx e\mathbf{E}t$ (blue arrow to dotted line), an additional field $\Delta\mathbf{B}_{\mathrm{eff}}$ (purple arrows) $\perp\mathbf{M}$ is felt. This field causes all spins to tilt in the same out-of-plane direction. For the case of a Rashba-like symmetry, the out-of-plane non-equilibrium carrier spin density that generates the Berry curvature antidamping SOT has a maximum for an applied electric field (anti-)parallel to the magnetization. **c**, For the case of a Rashba-like symmetry, the out-of-plane non-equilibrium carrier spin density is zero for $\mathbf{E}\perp\mathbf{M}$ because $\mathbf{B}_{\mathrm{eff}}^{\mathrm{eq}}$ and $\Delta\mathbf{B}_{\mathrm{eff}}$ are parallel to each other. **d**, The analogous physical phenomena for zero magnetization induces a tilt of the spin out of the plane that has opposite sign for momenta pointing to the left or right of the electric field, inducing in this way the intrinsic Berry curvature SHE[29].

now discuss our low-temperature (6 K) experiments in which we identify the presence of antidamping SOT due to the out-of-plane component of the non-equilibrium spin density in our in-plane magnetized (Ga,Mn)As samples. We follow the methodology of several previous experiments[2,11] and use current-induced ferromagnetic resonance (FMR) to investigate the magnitude and symmetries of the alternating fields responsible for resonantly driving the magnetization. In our experiment, illustrated schematically in Fig. 2a, a signal generator drives a microwave frequency current through a 4 μm × 40 μm microbar patterned from an 18-nm-thick (Ga,Mn)As epilayer with nominal 5% Mn-doping. A bias tee is used to measure the d.c. voltage across the sample, which is generated according to Ohm's law due to the product of the oscillating magnetoresistance (during magnetization precession) and the microwave current[42]. Solving the Landau–Lifshitz–Gilbert equation of motion for the magnetization for a small excitation field vector $(h_x,h_y,h_z)\exp[i\omega t]$, where h_i are the components of the excitation field amplitude and ω is its frequency, we find d.c. voltages containing symmetric (V_{S}) and antisymmetric (V_{A}) Lorentzian functions, shown in Fig. 2b. As the saturated magnetization of the sample is rotated, using $\theta_{\mathbf{M-E}}$ to indicate the angle from the current/bar direction, the in-plane and out-of-plane components of the excitation field are associated with V_{S} and V_{A} via

$$V_{\mathrm{S}} \propto h_z \sin 2\theta_{\mathbf{M-E}} \tag{6}$$

$$V_{\mathrm{A}} \propto -h_x \sin\theta_{\mathbf{M-E}} \sin 2\theta_{\mathbf{M-E}} + h_y \cos\theta_{\mathbf{M-E}} \sin 2\theta_{\mathbf{M-E}} \tag{7}$$

In this way we are able to determine, at a given magnetization orientation, the current-induced field vector. In Fig. 2c we show the angle dependence of V_{S} and V_{A} for an in-plane rotation of the

Table 1 | Angle $\theta_{\mathbf{M-E}}$ dependence of the Rashba and Dresselhaus contributions to S_z for electric fields along different crystal directions.

	Rashba: $S_z \sim$	Dresselhaus: $S_z \sim$
E‖[100]	$\cos\theta_{\mathbf{M-E}}$	$\sin\theta_{\mathbf{M-E}}$
E‖[010]	$\cos\theta_{\mathbf{M-E}}$	$-\sin\theta_{\mathbf{M-E}}$
E‖[110]	$\cos\theta_{\mathbf{M-E}}$	$\cos\theta_{\mathbf{M-E}}$
E‖[1-10]	$\cos\theta_{\mathbf{M-E}}$	$-\cos\theta_{\mathbf{M-E}}$

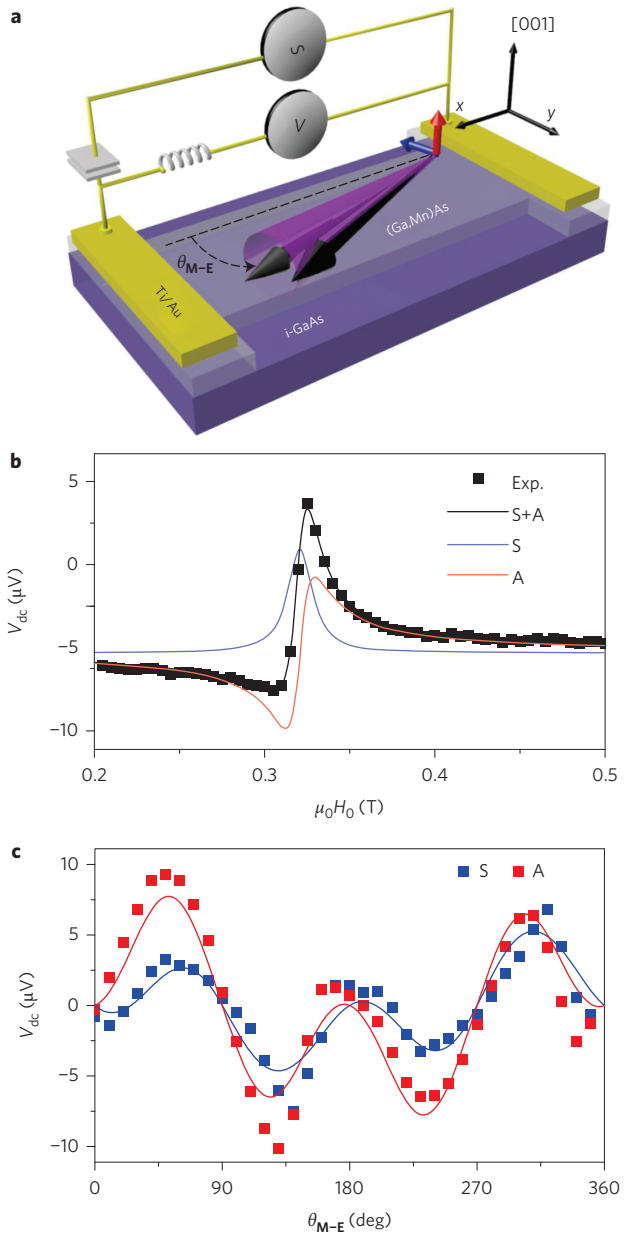

Figure 2 | Spin–orbit FMR experiment. a, Schematic of the sample, measurement set-up and magnetization precession. Microwave power passes through a bias-tee and into the (Ga,Mn)As microbar, which is patterned from a (Ga,Mn)As epilayer on an intrinsic-GaAs (i-GaAs) substrate, and placed inside a cryostat. The injected microwave current drives FMR, which is detected via the d.c. voltage V_{dc} across the microbar. We define θ_{M-E} as the angle of the static magnetization direction determined by the external magnetic field, measured from the current flow direction. Arrows represent in-plane (blue) and out-of-plane (red) components of the instantaneous non-equilibrium spin polarization induced by the microwave current that drives the magnetization. **b**, Typical spin–orbit FMR signal driven by an alternating current at 11 GHz and measured by V_{dc} as a function of external magnetic field. Data were fitted by a combination of symmetric (S) and antisymmetric (A) Lorentzian functions. **c**, Symmetric (blue data points and fitted line) and antisymmetric (red data points and fitted line) components of V_{dc} as a function of θ_{M-E} for current along the [100] direction.

magnetization for a microbar patterned in the [100] crystal direction. As described in Supplementary Note 1, voltages V_S and V_A are related to the alternating excitation field, using the micromagnetic parameters and anisotropic magnetoresistance of the sample. The in-plane field components, determined from V_A, are fitted by an M-independent current-induced field vector $(\mu_0 h_x, \mu_0 h_y) = (-91, -15)$ μT referenced to a current density of 1×10^5 A cm^{-2} (where μ_0 is the permeability of vacuum). Because V_S is non-zero, it is seen that there is also a significant h_z component of the current-induced field. Furthermore, V_S is not simply described by sin $2\theta_{M-E}$ and, correspondingly, h_z depends strongly on the in-plane orientation of the magnetization. To analyse the symmetry of the out-of-plane field we fit the angle dependence of V_S, finding for the [100] bar shown in (Fig. 2c) that $\mu_0 h_z = (13 + 95\sin\theta_{M-E} + 41\cos\theta_{M-E})$ μT.

We show measurements of eight samples, two patterned in each crystal direction and plot in Fig. 3 the resulting sin θ_{M-E} and cos θ_{M-E} coefficients of h_z. The corresponding in-plane fields are also shown; because these are approximately magnetization-independent they can be represented in Fig. 3 by a single vector. In the [100] bar we found that the sin θ_{M-E} coefficient of h_z (which according to the theoretical model originates in the Dresselhaus spin–orbit term) is greater than the cos θ_{M-E} coefficient related to the Rashba spin–orbit term (Table 1). If we examine the symmetries of h_z in our sample set, we find that they change in the manner expected for samples with a dominant Dresselhaus term, a trend that is in agreement with the in-plane fields. The angle dependence of h_z measured throughout our samples indicates an antidamping-like SOT with the theoretically predicted symmetries. Because the magnitude of the measured h_z is comparable to the in-plane fields (see Supplementary Table 1 for a detailed comparison), the anti-damping- and field-like SOTs are equally important for driving the magnetization dynamics in our experiment.

We note that the dominant Dresselhaus-like symmetry of h_z (confirmed in a series of samples patterned along different crystal directions from the same or different (Ga,Mn)As wafers) excludes that the measured V_S signals are artefacts of, for example, sample inhomogeneities. The homogeneity of the micromagnetic parameters in our (Ga,Mn)As materials has been independently confirmed in a previous magneto-optical FMR study[43], and the driving field homogeneity in our SOT–FMR measurements has been discussed in the Supplementary Information of ref. 11. The measurement artefacts of the frequency-dependent phase shifts between the alternating electrical current and the FMR generating field in experiments with waveguides adjacent to the sample[44] are absent in our SOT–FMR devices in which the current and field are intrinsically linked. To confirm this, we performed SOT–FMR measurements over a range of different frequencies and observed a constant ratio, within experimental error, of the antisymmetric and symmetric line shapes (Supplementary Note 2). On the other hand, we also note that the antidamping SOT fields inferred from the V_S signals have a non-zero error bar, the magnitude of which can be associated with the fitted weaker constant terms shown in Fig. 3. These are also listed in Supplementary Table 1, which shows that the constant terms, unlike the angle-dependent contributions, can fluctuate in amplitude and sign between nominally similar samples. We therefore attribute them to a random error from the measurement and fitting procedure.

Modelling of antidamping SOT in (Ga,Mn)As

To model the measured antidamping SOT, assuming its Berry curvature intrinsic origin, we start from the effective kinetic-exchange Hamiltonian describing (Ga,Mn)As (ref. 41): $H = H_{KL} + H_{strain} + H_{ex}$. We emphasize that the parameters of the Hamiltonian are taken to correspond to the measured (Ga,Mn)As samples and are not treated as free fitting parameters. $H_{ex} = J_{pd} c_{Mn} S_{Mn} \hat{\mathbf{M}} \cdot \mathbf{s}$, H_{KL} and H_{strain} refer to the strained Kohn–Luttinger Hamiltonian for the hole systems of GaAs (Supplementary Note 3), $\mathbf{s}$ is the hole spin operator, $S_{Mn} = 5/2$, c_{Mn} is the Mn density, and $J_{pd} = 55$ meV nm^3

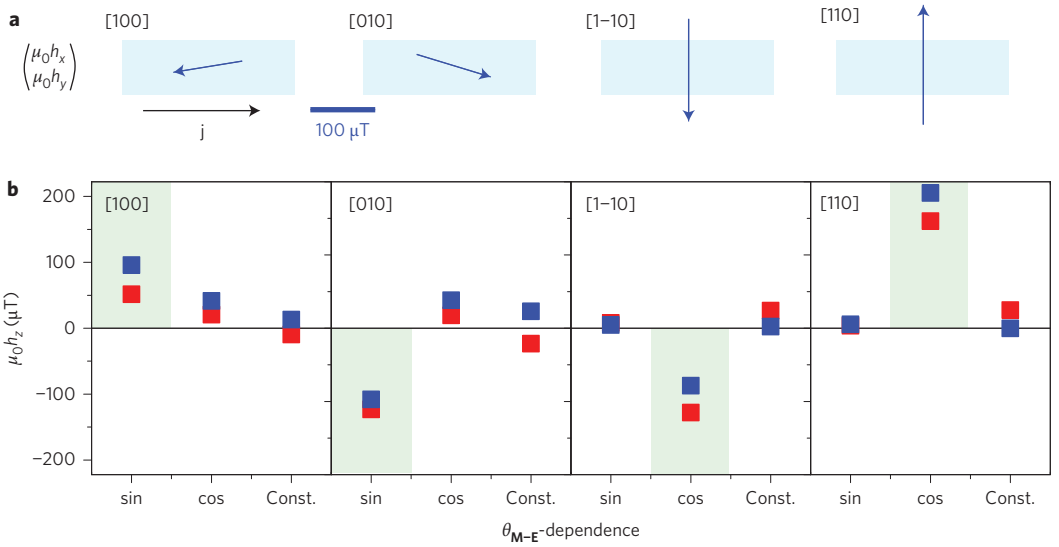

Figure 3 | In-plane and out-of-plane SOT fields. a, Direction and magnitude of the in-plane spin–orbit field (blue arrows) within the microbars (light blue rectangles). A single sample in each microbar direction is shown (corresponding to the same samples that yield the blue out-of-plane data points). The direction of the current is represented by *j*. **b**, Coefficients of the cos $\theta_{\mathbf{M-E}}$ and sin $\theta_{\mathbf{M-E}}$ fits to the angle dependence of the out-of-plane SOT field for the sample set. In this out-of-plane data, two samples are shown in each microbar direction and are distinguished by blue and red square data points. The symmetries expected for the antidamping SOT, on the basis of the theoretical model for the Dresselhaus term in the spin–orbit interaction, are shown by light green shading. All data are normalized to a current density of 1×10^5 A cm^{-2}.

is the kinetic-exchange coupling between the localized *d* electrons and the valence band holes. The Dresselhaus and Rashba symmetry parts of the strain Hamiltonian in the hole picture are given by

$$H_{\text{strain}} = -3C_4[s_x(\epsilon_{yy} - \epsilon_{zz})k_x + \text{c.p.}] - 3C_5[\epsilon_{xy}(k_y s_x - k_x s_y) + \text{c.p.}] \quad (8)$$

where ϵ_{ij} are the strain components, $C_4 = 10$ eV Å and we take $C_5 = C_4$ (refs 45,46), c.p. denotes cyclic permutations of the indices. These momentum-dependent H_{strain} terms are essential for the generation of SOT because they break the space-inversion symmetry. The momentum-dependent spin–orbit contribution to H_{KL} does not directly produce a SOT, but it does interfere with the linear in-plane momentum terms in H_{strain} to reduce the magnitude of the SOT and introduce higher harmonics in the $\theta_{\mathbf{M-E}}$ dependence of $\mu_0 h_z$. We have also performed additional calculations in which we replaced H_{KL} with a parabolic model with effective mass $m^* = 0.5m_e$ (m_e is the bare electron mass) and included the spin–orbit coupling only through the Rashba and Dresselhaus symmetry strain terms given by equation (8). The expected cos $\theta_{\mathbf{M-E}}$ or sin $\theta_{\mathbf{M-E}}$ symmetry without higher harmonics follows. In addition, a large increase of the amplitude of the effect is observed because the broken inversion symmetry spin texture does not compete with the centrosymmetric one induced by the large spin–orbit coupled H_{KL} term. This indicates that, for a system in which the dominant spin–orbit coupling is linear in momentum, our Berry curvature antidamping SOT will be largest.

In Fig. 4 we show calculations for our (Ga,Mn)As samples including the spin–orbit coupled H_{KL} term (full lines) term, or replacing it with the parabolic model (dashed lines). The non-equilibrium spin density induced by the Berry curvature effect is obtained from the Kubo formula[9]:

$$S_z = \frac{\hbar}{2\pi V}\text{Re}\sum_{\mathbf{k},a\neq b}\langle \mathbf{k},a|s_z|\mathbf{k},b\rangle\langle \mathbf{k},b|e\mathbf{E}\cdot\mathbf{v}|\mathbf{k},a\rangle[G^R_{\mathbf{k}a}G^A_{\mathbf{k}b} - G^R_{\mathbf{k}a}G^R_{\mathbf{k}b}] \quad (9)$$

where Green's functions $G^{\text{R}}_{\mathbf{k}a}(E)|_{E=E_{\text{F}}} \equiv G^{\text{R}}_{\mathbf{k}a} = 1/(E_{\text{F}} - E_{\mathbf{k}a} + i\Gamma)$, with the property $G^{\text{A}} = (G^{\text{R}})^*$. E_{F} is the Fermi energy and Γ is the disorder-induced spectral broadening, taken in the simulations to be 25 meV, which is a typical interband scattering rate obtained for the weakly compensated (Ga,Mn)As materials in the first-order Born approximation[41]. Note that in the disorder-free limit, equation (9) turns, for our model, into equation (5). (See also Supplementary Note 3 and ref. 9.) The relation between S_z and the effective magnetic field generating the Berry curvature SOT is given by $\mu_0 h_z = -(J_{\text{pd}}/g\mu_{\text{B}})S_z$, where μ_{B} is the Bohr magneton and $g = 2$ corresponds to the localized *d* electrons in (Ga,Mn)As (for more details on modelling see Supplementary Note 3).

The results of our calculations are compared in Fig. 4 with the experimental dependencies of h_z on $\theta_{\mathbf{M-E}}$ measured in the four microbar directions. As expected, the parabolic model calculations strongly overestimate the SOT field h_z. On the other hand, including the competing centrosymmetric H_{KL} term, which is present in the (Ga,Mn)As valence band, gives the correct order of magnitude of h_z as compared to experiment. Moreover, by including the H_{KL} term we can also explain the presence of higher harmonics in the $\theta_{\mathbf{M-E}}$ dependencies seen in experiment and reflecting the specific form of the carrier Hamiltonian in (Ga,Mn)As. This confirms that the experimentally observed antidamping SOT is of Berry curvature origin.

Implications for other systems

Learning from the analogy with the intrinsic anomalous Hall effect, first identified in (Ga,Mn)As and subsequently observed in a number of ferromagnets, we infer that our Berry curvature SOT is a generic phenomenon in spin–orbit coupled magnetic systems with broken space-inversion symmetry. In particular, we expect this antidamping Berry curvature SOT to be present in ferromagnet/paramagnet bilayer systems with broken structural inversion symmetry, and that it can contribute with a strength similar to that of the SHE–STT mechanism. The intrinsic SOT effect—identified in our work in the epilayer of (Ga,Mn)As with broken inversion symmetry in the crystal structure, and with the competing SHE–STT mechanism excluded by design—is associated with the

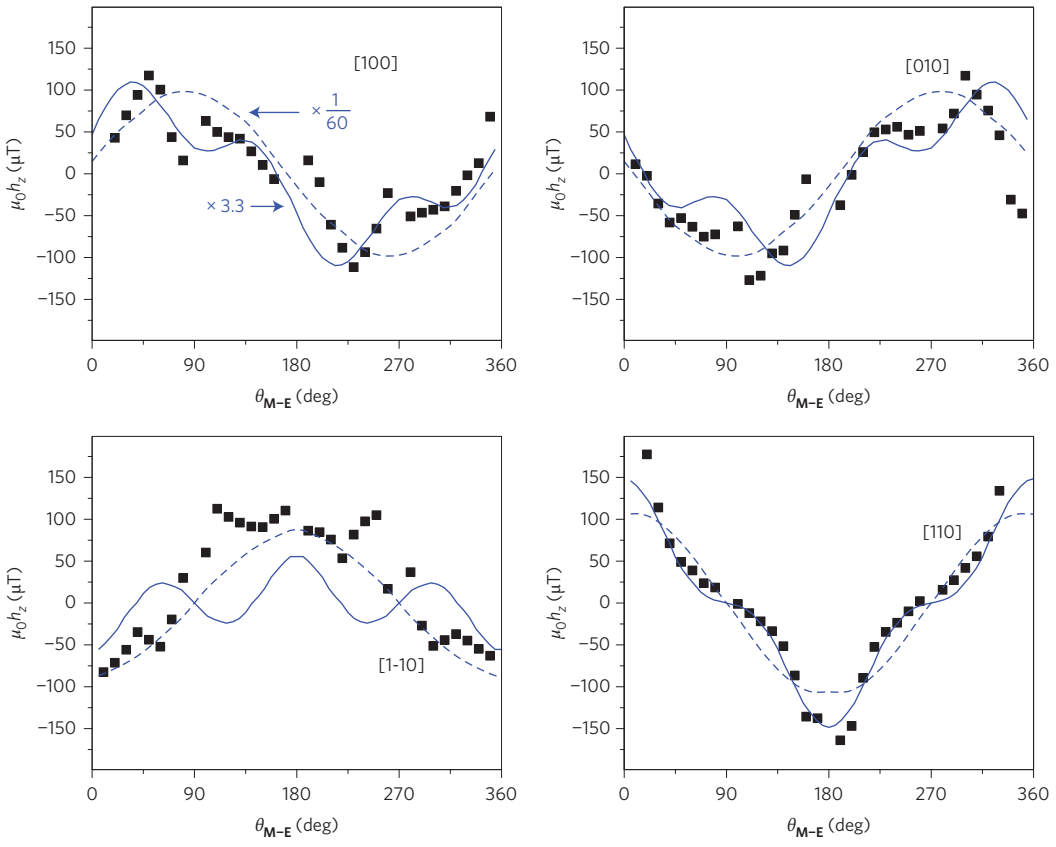

Figure 4 | Theoretical modelling of measured angular dependencies of SOT fields. Microscopic model calculation for the measured (Ga,Mn)As samples assuming Rashba ($\epsilon_{xy} = -0.15\%$) and Dresselhaus ($\epsilon_{xx} = -0.3\%$) strain. Solid blue lines correspond to calculations with the centrosymmetric H_{KL} term included in the (Ga,Mn)As Hamiltonian. Dashed blue lines correspond to replacing H_{KL} with the parabolic model. Both calculations are performed with a disorder broadening $\Gamma = 25$ meV. Black points indicate experimental data, where the fitting coefficients of the cos θ_{M-E} and sin θ_{M-E} first harmonics correspond to blue points in Fig. 3.

out-of-plane non-equilibrium spin density S_z. Our model calculations in the two-dimensional ferromagnet with Rashba spin–orbit coupling showed that S_z in the intrinsic SOT is proportional to the strength of the spin–orbit coupling and inversely proportional to the strength of the exchange field of the ferromagnet. We can compare this dependence on the spin–orbit and exchange couplings with the phenomenology of the competing SHE–STT mechanism. In ref. 37, it was shown that the intrinsic SHE current is proportional to the strength of the spin–orbit coupling in the paramagnetic 4*d*, 5*d* transition metals. The non-equilibrim spin density generating the adiabatic (antidamping) STT is proportional to the spin-density injection rate from the external polarizer and inversely proportional to the strength of the exchange field in the ferromagnet[47–49]. In the SHE–STT, the role of the spin-density injection rate from the external polarizer is played by the spin current generated by the SHE in the paramagnet. For the intrinsic SHE/antidamping (adiabatic) STT we can then conclude that it is generated by the non-equilibrium spin polarization, which is proportional to the spin–orbit strength in the paramagnet and inversely proportional to the exchange-field strength in the ferromagnet. For the intrinsic SOT we inferred the same proportionality to the spin–orbit strength and inverse proportionality to the exchange-field strength, but the SOT is considered to act within the few atomic layers forming the broken inversion-symmetry interface. Owing to proximity effects, however, the strength of the exchange field on either side of the interface can be comparable to the exchange field in the magnetic transition metal, and the same applies to the respective strengths of the interface and the bulk-paramagnet spin–orbit coupling. Therefore the SOT and SHE–STT can provide two comparably strong intrinsic mechanisms driving the in-plane current-induced spin dynamics in these technologically important transition-metal bilayers.

Methods

Materials. The 18-nm-thick ($Ga_{0.95}$,$Mn_{0.05}$)As epilayer was grown on a GaAs [001] substrate by molecular beam epitaxy, performed at a substrate temperature of 230 °C. It was subsequently annealed for 8 h at 200 °C. It has a Curie temperature of 132 K, a room-temperature conductivity of 387 Ω^{-1} cm^{-1} (which increases to 549 Ω^{-1} cm^{-1} at 5 K), and a carrier concentration at 5 K (determined by a high-magnetic-field Hall measurement) of 1.1×10^{21} cm^{-3}.

Devices. Two terminal microbars were patterned in different crystal directions by electron-beam lithography to have dimensions of 4 μm × 40 μm. These bars have a typical low-temperature resistance of 10 kΩ (Supplementary Table 2).

Experimental procedure. A pulse-modulated (at 789 Hz) microwave signal (at 11 GHz) with a source power of 20 dBm was transmitted down to cryogenic temperatures using low-loss semirigid cables. The microwave signal was launched onto a printed circuit board patterned with a coplanar waveguide and then injected into the sample via a bond wire. The rectification voltage, generated during microwave precession, was separated from the microwave circuit using a bias tee, amplified with a voltage amplifier and then detected with a lock-in amplifier. All measurements were performed with the samples at 6 K.

Calibration of microwave current. The resistance of a (Ga,Mn)As microbar depends on temperature, and therefore on Joule heating by an electrical current. The resistance change of the microbar due to Joule heating by a direct current was first measured. The resistance change was then measured as a function of applied microwave power. We assumed the same Joule heating (and therefore resistance change of the microbar) for the same direct and root-mean-square microwave currents, enabling us to calibrate the unknown microwave current against the known direct current.

For more details on the methods related to our SOT–FMR experiments and our (Ga,Mn)As materials see refs 11 and 43 and the Supplementary Information therein.

Received 30 May 2013; accepted 16 January 2014; published online 2 March 2014

References

1. Miron, I. M. *et al.* Perpendicular switching of a single ferromagnetic layer induced by in-plane current injection. *Nature* **476,** 189–193 (2011).
2. Liu, L. *et al.* Spin–torque switching with the giant spin Hall effect of tantalum. *Science* **336,** 555–558 (2012).
3. Edelstein, V. M. Spin polarization of conduction electrons induced by electric current in two-dimensional asymmetric electron systems. *Solid State Commun.* **73,** 233–235 (1990).
4. Bernevig, B. A. & Vafek, O. Piezo-magnetoelectric effects in p-doped semiconductors. *Phys. Rev. B* **72,** 033203 (2005).
5. Manchon, A. & Zhang, S. Theory of nonequilibrium intrinsic spin torque in a single nanomagnet. *Phys. Rev. B* **78,** 212405 (2008).
6. Manchon, A. & Zhang, S. Theory of spin torque due to spin–orbit coupling. *Phys. Rev. B* **79,** 094422 (2009).
7. Matos-Abiague, A. & Rodriguez-Suarez, R. L. Spin–orbit coupling mediated spin torque in a single ferromagnetic layer. *Phys. Rev. B* **80,** 094424 (2009).
8. Chernyshov, A. *et al.* Evidence for reversible control of magnetization in a ferromagnetic material by means of spin–orbit magnetic field. *Nature Phys.* **5,** 656–659 (2009).
9. Garate, I. & MacDonald, A. H. Influence of a transport current on magnetic anisotropy in gyrotropic ferromagnets. *Phys. Rev. B* **80,** 134403 (2010).
10. Endo, M., Matsukura, F. & Ohno, H. Current induced effective magnetic field and magnetization reversal in uniaxial anisotropy (Ga,Mn)As. *Appl. Phys. Lett.* **97,** 222501 (2010).
11. Fang, D. *et al.* Spin–orbit driven ferromagnetic resonance: a nanoscale magnetic characterization technique. *Nature Nanotech.* **6,** 413–417 (2011).
12. Miron, I. M. *et al.* Current-driven spin torque induced by the Rashba effect in a ferromagnetic metal layer. *Nature Mater.* **9,** 230–234 (2010).
13. Pi, U. H. *et al.* Tilting of the spin orientation induced by Rashba effect in ferromagnetic metal layer. *Appl. Phys. Lett.* **97,** 162507 (2010).
14. Hals, K. M. D., Brataas, A. & Tserkovnyak, Y. Scattering theory of charge-current-induced magnetization dynamics. *Europhys. Lett.* **90,** 47002 (2010).
15. Miron, I. M. *et al.* Fast current-induced domain-wall motion controlled by the Rashba effect. *Nature Mater.* **10,** 419–423 (2011).
16. Suzuki, T. *et al.* Current-induced effective field in perpendicularly magnetized Ta/CoFeB/MgO wire. *Appl. Phys. Lett.* **98,** 142505 (2011).
17. Kim, K-W., Seo, S-M., Ryu, J., Lee, K-J. & Lee, H-W. Magnetization dynamics induced by in-plane currents in ultrathin magnetic nanostructures with Rashba spin–orbit coupling. *Phys. Rev. B* **85,** 180404(R) (2012).
18. Pesin, D. A. & MacDonald, A. H. Quantum kinetic theory of current-induced torques in Rashba ferromagnets. *Phys. Rev. B* **86,** 014416 (2012).
19. Wang, X. & Manchon, A. Diffusive spin dynamics in ferromagnetic thin films with a Rashba interaction. *Phys. Rev. Lett.* **108,** 117201 (2012).
20. Haney, P. M., Lee, H-W., Lee, K-J., Manchon, A. & Stiles, M. D. Current induced torques and interfacial spin-orbit coupling: semiclassical modeling. *Phys. Rev. B* **87,** 174411 (2013).
21. Van der Bijl, E. & Duine, R. A. Current-induced torques in textured Rashba ferromagnets. *Phys. Rev. B* **86,** 094406 (2012).
22. Kim, J. *et al.* Layer thickness dependence of the current-induced effective field vector in Ta–CoFeB–MgO. *Nature Mater.* **12,** 240–245 (2012).
23. Garello, K. *et al.* Symmetry and magnitude of spin–orbit torques in ferromagnetic heterostructures. *Nature Nanotech.* **8,** 587–593 (2013).
24. Li, H., Wang, X., Dogan, F. & Manchon, A. Tailoring spin–orbit torque in diluted magnetic semiconductors. *Appl. Phys. Lett.* **102,** 192411 (2013).
25. Liu, L., Lee, O. J., Gudmundsen, T. J., Ralph, D. C. & Buhrman, R. A. Current-induced switching of perpendicularly magnetized magnetic layers using spin torque from the spin Hall effect. *Phys. Rev. Lett.* **109,** 096602 (2011).
26. Dyakonov, M. I. & Perel, V. I. Current-induced spin orientation of electrons in semiconductors. *Phys. Lett. A* **35,** 459–460 (1971).
27. Hirsch, J. E. Spin Hall effect. *Phys. Rev. Lett.* **83,** 1834–1837 (1999).
28. Murakami, S., Nagaosa, N. & Zhang, S-C. Dissipationless quantum spin current at room temperature. *Science* **301,** 1348–1351 (2003).
29. Sinova, J. *et al.* Universal intrinsic spin Hall effect. *Phys. Rev. Lett.* **92,** 126603 (2004).
30. Kato, Y. K., Myers, R. C., Gossard, A. C. & Awschalom, D. D. Observation of the spin Hall effect in semiconductors. *Science* **306,** 1910–1913 (2004).
31. Wunderlich, J., Kaestner, B., Sinova, J. & Jungwirth, T. Experimental observation of the spin Hall effect in a two dimensional spin–orbit coupled semiconductor system. *Phys. Rev. Lett.* **94,** 047204 (2005).
32. Jungwirth, T., Wunderlich, J. & Olejnik, K. Spin Hall effect devices. *Nature Mater.* **11,** 382–390 (2012).
33. Slonczewski, J. C. Current-driven excitation of magnetic multilayers. *J. Magn. Magn. Mater.* **159,** L1–L7 (1996).
34. Berger, L. Emission of spin waves by a magnetic multilayer traversed by a current. *Phys. Rev. B* **54,** 9353–9358 (1996).
35. Ralph, D., Stiles, M. & Bader, S. Current perspectives: spin transfer torques. *J. Magn. Magn. Mater.* **320,** 1189–1311 (2008).
36. Brataas, A., Kent, A. D. & Ohno, H. Current-induced torques in magnetic materials. *Nature Mater.* **11,** 372–381 (2012).
37. Tanaka, T. *et al.* Intrinsic spin Hall effect and orbital Hall effect in 4*d* and 5*d* transition metals. *Phys. Rev. B* **77,** 165117 (2008).
38. Engel, H-A., Rashba, E. I. & Halperin, B. I. Out-of-plane spin polarization from in-plane electric and magnetic fields. *Phys. Rev. Lett.* **98,** 036602 (2007).
39. Jungwirth, T., Niu, Q. & MacDonald, A. H. Anomalous Hall effect in ferromagnetic semiconductors. *Phys. Rev. Lett.* **88,** 207208 (2002).
40. Nagaosa, N., Sinova, J., Onoda, S., MacDonald, A. H. & Ong, N. P. Anomalous Hall effect. *Rev. Mod. Phys.* **82,** 1539–1592 (2010).
41. Jungwirth, T., Sinova, J., Mašek, J., Kučera, J. & MacDonald, A. H. Theory of ferromagnetic (III,Mn)V semiconductors. *Rev. Mod. Phys.* **78,** 809–864 (2006).
42. Tulapurkar, A. A. *et al.* Spin–torque diode effect in magnetic tunnel junctions. *Nature* **438,** 339–342 (2005).
43. Nemec, P. *et al.* The essential role of carefully optimized synthesis for elucidating intrinsic material properties of (Ga,Mn)As. *Nature Commun.* **4,** 1422 (2013).
44. Harder, M., Cao, Z. X., Gui, Y. S., Fan, X. L. & Hu, C. M. Analysis of the line shape of electrically detected ferromagnetic resonance. *Phys. Rev. B* **84,** 054423 (2011).
45. Silver, M., Batty, W., Ghiti, A. & OReilly, E. P. Strain-induced valence-subband splitting in III-V semiconductors. *Physica B* **46,** 6781–6788 (1992).
46. Stefanowicz, W. *et al.* Magnetic anisotropy of epitaxial (Ga,Mn)As on (113)A GaAs. *Phys. Rev. B* **81,** 155203 (2010).
47. Vanhaverbeke, A. & Viret, M. Simple model of current-induced spin torque in domain walls. *Phys. Rev. B* **75,** 024411 (2007).
48. Fernández-Rossier, J., Núñez, A. S., Abolfath, M. & MacDonald, A. H. Optical spin transfer in ferromagnetic semiconductors. Preprint at http://lanl.arXiv.org/cond-mat/0304492 (2003).
49. Nemec, P. *et al.* Experimental observation of the optical spin transfer torque. *Nature Phys.* **8,** 411–415 (2012).

Acknowledgements

The authors acknowledge support from the EU European Research Council (ERC) advanced grant no. 268066, from the Ministry of Education of the Czech Republic grant no. LM2011026, from the Grant Agency of the Czech Republic grant no. 14-37427G, from the Academy of Sciences of the Czech Republic Praemium Academiae, and support from US grants ONR-N000141110780, NSF-DMR-1105512 and NSF TAMUS LSAMP BTD award 1026774. A.J.F. acknowledges support from a Hitachi research fellowship. H.K. acknowledges financial support from the Japan Science and Technology Agency (JST).

Author contributions

Theory and data modelling were performed by T.J., E.K.V., L.P.Z., K.V. and J.S. Materials were prepared by V.N., R.P.C. and B.L.G. Sample preparation was performed by A.C.I. Experiments and data analysis were carried out by H.K., D.F., J.W. and A.J.F. The manuscript was written by T.J., A.J.F., H.K. and J.S., and project planning was performed by T.J., A.J.F., J.S. and H.K.

Additional information

Supplementary information is available in the online version of the paper. Reprints and permissions information is available online at www.nature.com/reprints. Correspondence and requests for materials should be addressed to A.J.F.

Competing financial interests

The authors declare no competing financial interests.